



# A new Mean Preserving Moving Least Squares method for Arbitrary Order Finite Volume schemes

Luis Ramírez<sup>a,\*</sup>, Laura Edreira<sup>a</sup>, Iván Couceiro<sup>a</sup>, Pablo Ouro<sup>b,c</sup>, Xesús Nogueira<sup>a</sup>, Ignasi Colominas<sup>a</sup>

<sup>a</sup>Group of Numerical Methods in Engineering-GMNI, Center for Technological Innovation in Construction and Civil Engineering-CITEEC, Civil Engineering School, Universidade da Coruña, Campus de Elviña, A Coruña, 15071, Spain

<sup>b</sup>Hydro-Environmental Research Centre, School of Engineering, Cardiff University, The Parade, Cardiff, CF24 3AA, UK

<sup>c</sup>School of Mechanical, Aerospace and Civil Engineering, University of Manchester, Manchester, M13 9PL, UK



## ARTICLE INFO

### Article history:

Available online 22 December 2022

### Keywords:

Finite Volume  
Moving Least Squares  
Mean Preserving  
Very high-order methods  
Compressible flows

## ABSTRACT

In this paper we propose a new arbitrary-order Finite Volume method for the numerical solution of the Euler and Navier-Stokes equations on unstructured grids. Arbitrary order is achieved using a modified Moving Least Squares reconstruction, which preserves the mean values of the conservative variables. Hence, the proposed scheme changes the traditional error functional of the MLS reconstruction in order to compare the cell-averaged values. Several benchmark problems are used to assess the proposed scheme's accuracy and performance, to show that arbitrary order of convergence can be achieved. Furthermore, the proposed method is applied to the numerical solution of the Navier-Stokes equations and its ability to simulate turbulent flows is verified.

© 2022 The Author(s). Published by Elsevier Inc.

This is an open access article under the CC BY-NC-ND license

(<http://creativecommons.org/licenses/by-nc-nd/4.0/>)

## 1. Introduction

Nowadays second-order schemes are still the common industry standard in CFD simulations. Unfortunately, the effect of irregular meshes decreases the accuracy of the simulations, since using those grids the effective order of the numerical schemes is between one and two. Thus, in order to obtain highly accurate solutions, a very fine mesh is required and very often it is not possible to obtain a grid-independent and reliable solution. It is believed that current standard methods are inadequate for some important scientific and engineering problems since they require a high amount of computational power. Thus, one question arises: Given an error considered acceptable, should we use a standard method with a fine resolution or a higher order method with a coarser one? Several authors [1,2] suggests that the second option is by far the most efficient if small errors are sought, by orders of magnitude.

In the last decades, an intense research in CFD has been focused on the development of very high-order methods in unstructured meshes [3,4]. This was specially due to their ability to achieve more accurate solutions, model certain small-scale flow structures, and the potential to significantly decrease the computational cost to obtain a given accuracy as they require coarser meshes.

\* Corresponding author.

E-mail address: [luis.ramirez@udc.es](mailto:luis.ramirez@udc.es) (L. Ramírez).

In Finite Volume schemes, one of the usual approaches to get high-order is the zero-mean approach, in which correction terms are added to the reconstruction of the variables in order to enforce the mean preserving condition on a pointwise framework [5–7]. Moving Least Squares (MLS) [8] reconstructions have been successfully used in Finite Volume schemes in a diverse variety of applications, from incompressible flows [9] to compressible flows including aeroacoustics [10,11] and turbulent flows [12]. However, this method cannot achieve convergence orders larger than three in non-stationary problems.

To overcome this drawback, a possible solution is to use a pseudo-mass matrix formulation, which relates the meanwise and pointwise frameworks. The mentioned formulation leads to an implicit time integration [13,14]. This approach has been shown to obtain arbitrary order of convergence. However, it considerably increases the computational cost.

A different approach is to use a mean value framework. In this category of Finite Volume methods are the  $k$ -exact reconstruction [15,16], polynomial reconstruction [17,18], ADER schemes [19,20], WENO reconstruction [21–24] or recently the CWENO reconstruction [25], among others.

In this work, we propose an alternative MLS reconstruction, that in a finite volume framework, is able to reach arbitrary order of convergence using explicit time integration schemes without additional computational cost. This novel formulation relies in the enforcement of the mean preserving condition in the reconstruction procedure.

This paper is organized as follows. First, the governing equations and the numerical basis are presented in Section 2. Then, the solution reconstruction is discussed in Section 3, where the proposed Mean-Preserving reconstruction is presented. Next, the discretization of the flux is indicated in Section 4. Afterward, Section 5 explains the time discretization used in this work. Furthermore, numerical test cases are presented in Section 7 to validate the accuracy of the new reconstruction procedure on a Finite Volume framework. Finally, conclusions are drawn in Section 8.

## 2. Governing equations and Numerical Discretization

The conservative form of Navier-Stokes equations for a compressible time-dependent flow reads as

$$\frac{\partial \mathbf{U}}{\partial t} + \nabla \cdot (\mathbf{F}^H - \mathbf{F}^E) = \mathbf{S} \tag{1}$$

$\mathbf{U}$  is the vector of conservative variables,  $\mathbf{F}^H$  is the inviscid or hyperbolic-like fluxes,  $\mathbf{F}^E$  is the viscous or diffusive-like fluxes and  $\mathbf{S}$  is the source term. For three-dimensional cases, equations (2),(3) and (4) define the vectors of variables and fluxes.

$$\mathbf{U} = \begin{pmatrix} \rho \\ \rho u \\ \rho v \\ \rho w \\ \rho E \end{pmatrix}, \tag{2}$$

where  $\rho$ ,  $\mathbf{u} = (u, v, w)$  and  $E$  are the density, velocity and total energy of the fluid, respectively. The convective fluxes are given by

$$\mathbf{F}_x^H = \begin{pmatrix} \rho u \\ \rho u^2 + p \\ \rho uv \\ \rho uw \\ \rho Eu + pu \end{pmatrix}, \quad \mathbf{F}_y^H = \begin{pmatrix} \rho v \\ \rho uv \\ \rho v^2 + p \\ \rho vw \\ \rho Ev + pv \end{pmatrix}, \tag{3}$$

$$\mathbf{F}_z^H = \begin{pmatrix} \rho w \\ \rho wu \\ \rho wv \\ \rho w^2 + p \\ \rho Ew + pw \end{pmatrix}$$

where  $p$  denotes the fluid's pressure. The viscous fluxes are given by the following expression

$$\mathbf{F}_x^E = \begin{pmatrix} 0 \\ \tau_{xx} \\ \tau_{xy} \\ \tau_{xz} \\ \tau_x \cdot \mathbf{u} \end{pmatrix}, \quad \mathbf{F}_y^E = \begin{pmatrix} 0 \\ \tau_{yx} \\ \tau_{yy} \\ \tau_{yz} \\ \tau_y \cdot \mathbf{u} \end{pmatrix}, \quad \mathbf{F}_z^E = \begin{pmatrix} 0 \\ \tau_{zx} \\ \tau_{zy} \\ \tau_{zz} \\ \tau_z \cdot \mathbf{u} \end{pmatrix}, \tag{4}$$

where  $\boldsymbol{\tau}$  represents the viscous stress tensor and it has the following expression

$$\boldsymbol{\tau} = \mu(\nabla(\mathbf{u}) + \nabla(\mathbf{u})^T) - \frac{2}{3}\mu\nabla \cdot (\mathbf{u})\mathbf{I}$$

The Euler system of equations is obtained particularizing the previous system for inviscid fluids, i.e.,  $\mathbf{F}^E = \mathbf{0}$ .

The computational domain is divided into a finite number of cells (control volumes). The system of conservation laws defined in (1) is integrated in each cell  $I$

$$\int_{\Omega_I} \frac{\partial \mathbf{U}}{\partial t} d\Omega + \int_{\Omega_I} \nabla \cdot (\mathbf{F}^H - \mathbf{F}^E) d\Omega - \int_{\Omega_I} \mathbf{S} d\Omega = \mathbf{0} \tag{5}$$

where  $\Omega_l$  represents the computational domain associated to the cell  $l$ : volume, area, or length, depending on the considered dimensions. The Finite Volume Method analyzes the mean value of the conservative variables in each cell or control volume, which reads as

$$\bar{\mathbf{U}}_l = \frac{1}{\Omega_l} \int_{\Omega_l} \mathbf{U} \, d\Omega. \tag{6}$$

The time derivative of equation (6) reads

$$\frac{\partial \bar{\mathbf{U}}_l}{\partial t} = \frac{1}{\Omega_l} \int_{\Omega_l} \frac{\partial \mathbf{U}}{\partial t} \, d\Omega. \tag{7}$$

Introducing equation (7) in equation (5) and applying the Gauss' Theorem we arrive to

$$\Omega_l \frac{\partial \bar{\mathbf{U}}_l}{\partial t} = \int_{\Gamma_l} (\mathbf{F}^E - \mathbf{F}^H) \cdot \mathbf{n} \, d\Gamma + \int_{\Omega_l} \mathbf{S} \, d\Omega \tag{8}$$

$\Gamma_l$  refers to the interface between cells (faces in 3D, edges in 2D and points in 1D) and  $\mathbf{n}$  is outward normal vector of  $\Gamma_l$ . The resulting flux integral is approximated using a numerical quadrature to each edge/faces. The numerical quadrature must have at least the same order as the method to be constructed. In this work, we have used the Gauss-Legendre quadrature of suitable order of accuracy, leading to

$$\Omega_l \frac{\partial \bar{\mathbf{U}}_l}{\partial t} = \sum_{j=1}^{N_f} \sum_{ig=1}^{N_G} [(\mathbf{F}^E - \mathbf{F}^H) \cdot \hat{\mathbf{n}}_j]_{ig} \mathcal{W}_{ig} + \int_{\Omega_l} \mathbf{S} \, d\Omega. \tag{9}$$

In equation (9), the number of edges/faces of  $\Gamma_l$  is denoted by  $N_f$ , each one is discretized with  $N_G$  quadrature points, and each point  $ig$  has its corresponding associated weight  $\mathcal{W}_{ig}$  and  $\hat{\mathbf{n}}_j$  refers to the outward normal  $\mathbf{n}$  multiplied with the edge/face's length/area.

To obtain a high-order accuracy method, it is necessary to estimate the flux at each integration point using a high-order reconstruction of the variables. In this paper, we present a new Mean Preserving Moving Least Squares (MP-MLS) reconstruction that achieves arbitrary order of accuracy.

### 3. Solution Reconstruction

The most noticeable component of a high-order accurate finite-volume solver is the variables reconstruction inside each cell. In this sense, the reconstruction of the variables can be based on  $k$ -exact [15,16] or Moving Least Squares [7] reconstructions, among others [21,22,26]. This work will focus on the MLS reconstructions, first briefly describing the method and then presenting a modification of the error functional which leads to the new Mean Preserving Moving Least Squares Method (MP-MLS).

#### 3.1. Moving Least Squares Method

The Moving Least Squares approximation was conceived by Lancaster and Salkauskas [8] aiming to reconstruct a given function from scattered point-wise data. This method is a widely used reconstruction method and it has been extensively analyzed and used by the meshless community [27–31] where MLS is employed to obtain the shape functions of the Diffuse Element Method (DLM) [32]. In [33] the Element-Free Galerkin (EFG) method was formulated combining the MLS approach with the Galerkin method. The use of the MLS approximation on a Finite Volume Method (FV-MLS) was introduced in the literature [7,34] with the primary purpose of achieving a high-order reconstruction of the variables. In the following, we will describe the fundamentals of MLS, which is the basis of the proposed method.

Given a set of point values of an arbitrary function  $u(\mathbf{x})$ , the MLS method approximates the function from the scattered point-wise values  $u(\mathbf{x}_j)$  by the function  $u^h(\mathbf{x})$

$$u(\mathbf{x}) \approx u^h(\mathbf{x}) = \mathbf{p}^T(\mathbf{x}) \boldsymbol{\alpha}(\mathbf{x}) \tag{10}$$

where the polynomial basis,  $\mathbf{p}(\mathbf{x})$ , is defined in 1D as  $\mathbf{p}(\mathbf{x}) = \{x^{m_1-1}\}_{m_1=1,\dots,m}$  and the vector of reconstruction coefficients are given by  $\boldsymbol{\alpha}(\mathbf{x}) = \{\alpha_i\}_{i=1,\dots,m}$ . These coefficients are calculated by minimizing an error functional of weighted residual that uses the approximated field function  $u^h(\mathbf{x})$  and the field function  $u(\mathbf{x})$  at the compact support  $\Omega_{\mathbf{x}}$

$$J(\boldsymbol{\alpha}(\mathbf{x})) = \int_{\mathbf{x}_k \in \Omega_{\mathbf{x}}} W(\mathbf{x} - \mathbf{x}_k, h) [u(\mathbf{x}_k) - \mathbf{p}^T(\mathbf{x}_k) \boldsymbol{\alpha}(\mathbf{x})]^2 \, d\Omega_{\mathbf{x}}. \tag{11}$$

The kernel function  $W(\mathbf{x} - \mathbf{x}_k, h)$  is centered in a point  $\mathbf{x}$ , and weights the importance in the approximation of the points inside the stencil. The stencil is determined by  $h$  (the smoothing length), leading to a compact cloud of points. The choice of the kernel function is an essential part in the definition of the method since it determines the approximation properties of

the MLS method, as described in [7,10,35]. Among the broad-spectrum of kernel functions that can be found in the literature [36–38], the exponential kernel is used in this work, defined as

$$W_k(\mathbf{x}_k, \mathbf{x}, s_x) = \frac{e^{-\left(\frac{|\mathbf{x}_k - \mathbf{x}|}{c}\right)^2} - e^{-\left(\frac{h}{c}\right)^2}}{1 - e^{-\left(\frac{h}{c}\right)^2}} \tag{12}$$

for each of the  $n_x$  points inside the compact support, where  $c = \frac{h}{s_x}$ ,  $h$  is the smoothing length defined as  $h = 2 \max(|\mathbf{x}_j - \mathbf{x}|)$ . The shape parameter,  $s_x$ , modifies the weighting properties of the kernel, and consequently also the properties of the numerical method [11]. Throughout this work, it is set to  $s_x = 4$ .

The minimization of the error functional given by (11) and the evaluation of the integrals using the neighboring cells leads to

$$\boldsymbol{\alpha}(\mathbf{x}) = \mathbf{M}^{-1}(\mathbf{x})\mathbf{P}_{\Omega_x}\mathbf{W}(\mathbf{x})\mathbf{u}_{\Omega_x} \tag{13}$$

where  $\mathbf{u}_{\Omega_x}$  is a vector of size  $n_x$  with point-wise values of  $u(\mathbf{x})$  for each point of the stencil  $\Omega_x$ , the matrix  $\mathbf{P}_{\Omega_x}$  with dimensions  $m \times n_x$  represents the basis functions evaluated at the nodes inside the compact support and the diagonal matrix  $\mathbf{W}(\mathbf{x})$  defines the kernel function values for the stencil cells and its dimension is  $n_x \times n_x$ . The moment matrix  $\mathbf{M}(\mathbf{x})$  (dimension  $m \times m$ ) depends exclusively on the number of elements of the basis function vector and not on the number of points employed,  $n_x$ , as follows

$$\mathbf{M}(\mathbf{x}) = \mathbf{P}_{\Omega_x}\mathbf{W}(\mathbf{x})\mathbf{P}_{\Omega_x}^T. \tag{14}$$

The resulting approximation,  $u^h(\mathbf{x})$ , can be written in terms of the MLS shape functions,  $\mathbf{N}(\mathbf{x})$ , as

$$u(\mathbf{x}) \approx u^h(\mathbf{x}) = \mathbf{p}^T(\mathbf{x})\mathbf{M}^{-1}(\mathbf{x})\mathbf{P}_{\Omega_x}\mathbf{W}(\mathbf{x})\mathbf{u}_{\Omega_x} = \mathbf{N}^T(\mathbf{x})\mathbf{u}_{\Omega_x}. \tag{15}$$

It is worth pointing out that the order of the MLS approximation is determined by the polynomial basis. Notably, locally evaluating the basis function prevents a severely ill-conditioned  $\mathbf{M}$  matrix, as suggested in [7]. That is, if the shape function vector,  $\mathbf{N}(\mathbf{x})$ , is evaluated at  $\mathbf{x}_i$ , the basis function will be evaluated at  $\mathbf{p}\left(\frac{\mathbf{x} - \mathbf{x}_i}{h}\right)$ , i.e.

$$\mathbf{N}^T(\mathbf{x}_i) = \mathbf{p}^T(0)\mathbf{M}^{-1}(\mathbf{x}_i)\mathbf{P}_{\Omega_{\mathbf{x}_i}}\mathbf{W}(\mathbf{x}_i). \tag{16}$$

In order to compute the high-order approximate derivatives of  $u(\mathbf{x})$ , we have to compute the derivatives of  $\mathbf{N}(\mathbf{x})$ . We refer the reader to [7,10,13] for a full description of these computations.

### 3.2. A new Mean Preserving Moving Least Squares reproducing kernel approximations

As previously stated in equation (11), the Moving Least Squares method uses the point-wise values stored at the cell-centroid in the cell-centered control volumes. Note that if the scheme updates the cell-averaged values of the sought function  $u(\mathbf{x})$  at each time step, the prior error functional compares the point-wise value of the reconstruction,  $u^h(\mathbf{x}_k) = \mathbf{p}^T(\mathbf{x}_k)\boldsymbol{\alpha}(\mathbf{x})$ , with the cell-averaged stored values,  $\bar{u}(\mathbf{x}_k)$ .

In a higher-order representation of the solution (that is, for convergence orders > 2nd order), cell-averaged values differ from the point-wise values at the centroid. Remarkably, regardless of the scheme, cell-averaged values have to be used to reach the expected accuracy order.

The requirement of the Mean Preserving condition on the conservative variables of the Finite Volume method is crucial to attain higher formal order of accuracy in unsteady problems. To ensure this, the resulting reconstruction  $u^h(\mathbf{x})$ , must satisfy that the cell-average of the reconstruction function  $u^h(\mathbf{x})$  and the original function  $u(\mathbf{x})$  over a control volume  $k$  must be the same, that is

$$\bar{u}^h(\mathbf{x}_k) = \frac{1}{\Omega_k} \int_{\Omega_k} u^h(\mathbf{x})d\Omega_k \approx \frac{1}{\Omega_k} \int_{\Omega_k} u(\mathbf{x})d\Omega_k = \bar{u}_{\Omega_k}. \tag{17}$$

Thus, the Mean Preserving condition is not directly enforced in the MLS method. In this reconstruction a correction must be incorporated in order to achieve a third-order method as it was performed in previous works [7,39,40]. To solve this drawback, in this work we propose a modified MLS formulation that verifies the Mean Preserving condition. We start by modifying the MLS error functional given by equation (11) to directly enforce this condition. The proposed Mean Preserving MLS (MP-MLS) functional reads as

$$J(\boldsymbol{\alpha}(\mathbf{x})) = \int_{\mathbf{x}_k \in \Omega_x} W(\mathbf{x} - \mathbf{x}_k, h) \left[ \bar{u}(\mathbf{x}_k) - \frac{1}{\Omega_k} \int_{\Omega_k} \mathbf{p}^T(\mathbf{x}_k)\boldsymbol{\alpha}(\mathbf{x})d\Omega_k \right]^2 d\Omega_x. \tag{18}$$

This modification aims at minimizing the reconstruction error of the mean functions of the control volume  $I$  and the neighboring control volumes inside the compact support,  $\Omega_x$  (the stencil of cell  $I$ ). In order to achieve it, the MP-MLS functional compares cell-averaged values exclusively: on the one hand, the solution at the cell-centroids  $\bar{u}(\mathbf{x}_k)$ , on the other hand, the reconstruction values at the cell-centroids  $\bar{u}^h(\mathbf{x}_k)$ .

Similar to what it is done in the MLS method, we will minimize the error functional and evaluate the integrals using the cell centroids of the stencil as quadrature points. Consequently, equation (18) becomes

$$\sum_{k=1}^{n_x} W(\mathbf{x} - \mathbf{x}_k, h) \hat{\mathbf{p}}^T(\mathbf{x}_k) \boldsymbol{\alpha} \hat{p}_j(\mathbf{x}_k) = \sum_{k=1}^{n_x} W(\mathbf{x} - \mathbf{x}_k, h) \tilde{\mathbf{u}}(\mathbf{x}_k) \hat{p}_j(\mathbf{x}_k) \tag{19}$$

where  $\hat{\mathbf{p}}(\mathbf{x}_k)$  is defined as the  $k$ -cell-averaged value of  $\mathbf{p}(\mathbf{x})$ , and  $j$  refers to the  $j$ -element of the vector. Mathematically, it can be expressed by

$$\hat{\mathbf{p}}(\mathbf{x}_k) = \frac{1}{\Omega_k} \int_{\Omega_k} \mathbf{p}(\mathbf{x}) d\Omega_k, \quad \hat{p}_j(\mathbf{x}_k) = \frac{1}{\Omega_k} \int_{\Omega_k} p_j(\mathbf{x}) d\Omega_k. \tag{20}$$

Writing the system of equations defined in (19) in matrix form and rearranging leads to

$$\boldsymbol{\alpha}(\mathbf{x}) = \hat{\mathbf{M}}^{-1}(\mathbf{x}) \hat{\mathbf{P}}_{\Omega_x} \mathbf{W}(\mathbf{x}) \tilde{\mathbf{u}}_{\Omega_x} \tag{21}$$

where  $\tilde{\mathbf{u}}_{\Omega_x}$  contains the  $n_x$  cell-averaged values of  $u(\mathbf{x})$ , the matrix  $\mathbf{W}(\mathbf{x})$  includes the values of the weighted function for the neighboring cells of the stencil, the matrix  $\hat{\mathbf{P}}_{\Omega_x}$  represents the cell-averaged basis functions inside the compact support and the moment matrix  $\hat{\mathbf{M}}(\mathbf{x})$  is defined similarly to  $\mathbf{M}(\mathbf{x})$  in equation (14) as

$$\hat{\mathbf{M}}(\mathbf{x}) = \hat{\mathbf{P}}_{\Omega_x} \mathbf{W}(\mathbf{x}) \hat{\mathbf{P}}_{\Omega_x}^T \tag{22}$$

with

$$\hat{\mathbf{P}}_{\Omega_x} = \begin{pmatrix} 1 & \hat{p}_2(x_1) & \dots & \hat{p}_m(x_1) \\ \vdots & \vdots & \ddots & \vdots \\ 1 & \hat{p}_2(x_{n_x}) & \dots & \hat{p}_m(x_{n_x}) \end{pmatrix}. \tag{23}$$

Finally, the reconstructed function can be expressed using the Mean Preserving shape functions  $\hat{\mathbf{N}}(\mathbf{x})$  as

$$\tilde{\mathbf{u}}(\mathbf{x}) \approx \tilde{\mathbf{u}}^h(\mathbf{x}) = \hat{\mathbf{p}}^T(\mathbf{x}) \hat{\mathbf{M}}^{-1}(\mathbf{x}) \hat{\mathbf{P}}_{\Omega_x} \mathbf{W}(\mathbf{x}) \tilde{\mathbf{u}}_{\Omega_x} = \hat{\mathbf{N}}^T(\mathbf{x}) \tilde{\mathbf{u}}_{\Omega_x}. \tag{24}$$

Since the proposed reconstruction of the variables satisfies the mean preserving condition, the variables can be directly computed at the integration points as

$$\tilde{\mathbf{u}}^h(\mathbf{x}_{ig}) = \hat{\mathbf{N}}^T(\mathbf{x}_{ig}) \tilde{\mathbf{u}}_{\Omega_x}. \tag{25}$$

#### 4. Discretization of the flux

The hyperbolic fluxes,  $\mathbf{F}^H$ , must be evaluated at each integration point as expressed in (9). To obtain those values we use a “broken” reconstruction approach of the variables  $\mathbf{U}$  applying the MP-MLS to obtain the high-order reconstruction from each control volume that shares the integration point. This flux is approximated using a numerical flux that solves the Riemann problem, that is,  $\mathbf{F}^H \cdot \hat{\mathbf{n}} \approx \mathcal{H}(\mathbf{U}^+, \mathbf{U}^-)$ , where the  $\mathbf{U}^+$  and  $\mathbf{U}^-$  denotes the reconstruction variables of cells sharing the interface where the integral is performed.

This work considers two different Riemann solvers, depending on the numerical example. Note that this choice is arbitrary and it depends on the preferences of the user. Here we have used both Rusanov’s and Roe’s fluxes. In all the problems except in the Taylor-Green vortex (TGV), Rusanov’s HLL flux [41] is used, which is given by

$$\mathcal{H}_{ig} = \frac{1}{2} (\mathbf{F}^H(\mathbf{U}_{ig}^+) + \mathbf{F}^H(\mathbf{U}_{ig}^-)) \cdot \hat{\mathbf{n}} - \frac{1}{2} S^+ \Delta(\mathbf{U}) \tag{26}$$

where  $S^+$  denotes the maximum eigenvalue and  $\Delta(\mathbf{U}) = (\mathbf{U}_{ig}^+ - \mathbf{U}_{ig}^-)$ . For the TGV test cases, we have chosen the Roe’s flux different splitting [42] since it is less dissipative than Rusanov’s flux. Roe’s flux can be expressed as

$$\mathcal{H}_{ig} = \frac{1}{2} (\mathbf{F}^H(\mathbf{U}_{ig}^+) + \mathbf{F}^H(\mathbf{U}_{ig}^-)) \cdot \hat{\mathbf{n}} - \frac{1}{2} \sum_{k=1}^4 \tilde{\alpha}_k |\tilde{\lambda}_k| \tilde{\mathbf{r}}_k \tag{27}$$

where  $\tilde{\mathbf{r}}_k$  are the eigenvectors and  $\tilde{\lambda}_k$  are the eigenvalues of the approximated Jacobian  $\tilde{\mathbf{J}}(\mathbf{U}^+, \mathbf{U}^-)$ .

For both fluxes, the Riemann states are computed on each integration point using equation (25) from cells sharing the point/edge/face where the flux integral is performed in equation (9). We note that this is different from the usual approach of using Taylor reconstructions.

The diffusive-like fluxes,  $\mathbf{F}^E$ , can be directly evaluated at the interfaces by making a reconstruction centered at each integration point and at each time step in a continuous approach [7,9]. However, the numerous integration points would substantially increase the computational cost. Thus, the viscous fluxes are obtained by averaging the directly evaluated MP-MLS reconstructions at the integration points centered at the neighboring cells-centroids sharing the interface, i.e.

$$\mathbf{F}_{ig}^E = \frac{1}{2} (\mathbf{F}_{ig}^{E+} + \mathbf{F}_{ig}^{E-}) \tag{28}$$

where the derivatives needed for the computation of the diffusive fluxes are computed using the MP-MLS reconstruction.

### 5. Time Integration

In this work, the chosen time integration scheme is a TVD third-order Runge-Kutta [43]. The time step  $\Delta t$  employed is determined, unless stated otherwise, on the CFL condition given by

$$\Delta t = \text{CFL} \cdot \min \left( \frac{\Omega_I^{1/D}}{\lambda_I} \right) \cdot \left( \frac{N_{min}}{N} \right)^{\max(0, \frac{k}{3}-1)/D} \tag{29}$$

where  $D$  refers to the dimensions of the problem,  $N$  is the spatial discretization employed (number of cells),  $N_{min}$  is the spatial discretization employed in the coarser mesh for that specific problem and  $k$  is the reconstruction order. Since the time discretization is third order and the spatial discretization is arbitrary, following [44] we scale the  $\Delta t$  with expression (29) to ensure that errors due the temporal integration converge at least with the same order as the spatial discretization. Note that  $\lambda_I$  refers to the maximum eigenvalue, i.e.,  $\lambda_I = \|\mathbf{v}_i\| + c_i$  for the Euler equation.

### 6. The Finite Volume method based on MP-MLS (FV-MP-MLS)

As commented previously, a high-order reconstruction of the variables inside each cell is required to get a high-order scheme. In the traditional Finite Volume method based on Moving Least Squares (FV-MLS), the high-order reconstruction of the variables is performed using a Taylor series expansion as

$$u^h(x) = u_i + \frac{\partial u}{\partial x} \Big|_i (x - x_i) + \frac{1}{2} \frac{\partial^2 u}{\partial x^2} \Big|_i \left[ (x - x_i)^2 - \frac{1}{\Omega_I} \int_{\Omega_I} (x - x_i)^2 dx \right] \tag{30}$$

where the needed derivatives are computed using MLS. Note that in expression (30), a correction term is included in order to satisfy the mean preserving condition expressed in (6). Using this corrected reconstruction, a third-order finite volume can be obtained for unsteady problems [7,39,40].

In the proposed Finite Volume method based on Mean Preserving Moving Least Squares (FV-MP-MLS), the Taylor series expansion is no more required to obtain the reconstructed values of the variables at integration points, since we already have a very accurate and higher order reconstruction performed with MLS which in addition fulfills the Mean Preserving condition (17). Thus, the resulting variable reconstruction  $\bar{u}^h$  is straightforwardly computed, i.e.

$$\bar{u}^h(\mathbf{x}) = \hat{\mathbf{N}}^T(\mathbf{x}) \bar{\mathbf{u}}_{\Omega_x}. \tag{31}$$

Moreover, the diffusive-like fluxes are also evaluated directly with the MP-MLS reconstruction at the integration points using equation (28).

### 7. Numerical Results

In this section we present the numerical results for several test cases obtained with the proposed formulation.

#### 7.1. Analysis of numerical dissipation and dispersion

In this first test case, we analyze behavior and properties of the FV-MP-MLS scheme. To this end, we will analyze the dissipation and dispersion properties for the 1D convection equation, given by

$$\frac{\partial U}{\partial t} + a \frac{\partial U}{\partial x} = 0. \tag{32}$$

The computational domain is  $0 \leq x \leq 2\pi$  and periodic boundary conditions are prescribed. The initial condition is given by a harmonic function as

$$U_0 = g(0)e^{ikx} = \sum_{q=1}^F g_q(0)e^{ik_q x} \tag{33}$$

where the analytic solution of the problem is

$$U(x, t) = g(t)e^{ikx} = \sum_{q=1}^F g_q(0)e^{ik_q(x-at)} \tag{34}$$

where

$$g(t) = g(0)e^{-iak t}. \tag{35}$$

The finite volume discretization for equation (32) can be written as

$$\frac{\partial \bar{U}_I}{\partial t} = -\frac{a}{\Delta x} \left( U_{I+\frac{1}{2}}^h - U_{I-\frac{1}{2}}^h \right) \tag{36}$$

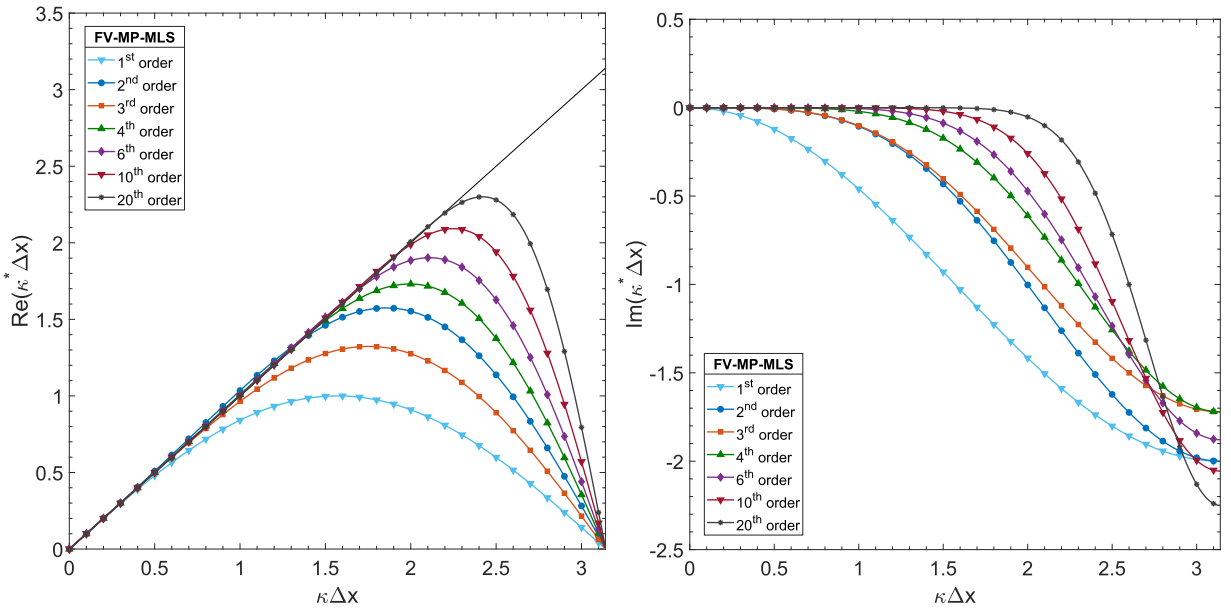


Fig. 1. Analysis of numerical dissipation and dispersion of FV-MP-MLS: The dispersion (left) and dissipation (right) curves are represented for reconstruction orders ranging from 1<sup>st</sup> to 20<sup>th</sup>.

where the exact value of the left term reads

$$\frac{\partial \bar{U}_l}{\partial t} = \frac{\partial g(t)}{\partial t} \frac{1}{\Delta x} \int_{x_l}^{x_R} e^{i\kappa x} dx = \frac{-ag(t)}{\Delta x} (e^{i\kappa x_R} - e^{i\kappa x_l}) \tag{37}$$

and the right term can be expressed by the proposed MP-MLS reconstruction as

$$\begin{aligned} \frac{-a}{\Delta x} (\bar{U}_{l+\frac{1}{2}}^h - \bar{U}_{l-\frac{1}{2}}^h) &= \frac{-ag(t)}{i\kappa \Delta x} (e^{i\kappa x_R} - e^{i\kappa x_l}) Z_1 = \\ &= \frac{-a}{\Delta x} (\hat{N}^T(x_{l+\frac{1}{2}}) \bar{U}_{\Omega_x} - \hat{N}^T(x_{l-\frac{1}{2}}) \bar{U}_{\Omega_x}) = \\ &= \frac{-ag(t)}{i\kappa \Delta x} \sum_{l=-P}^Q N_{(l+1)} (e^{i\kappa l \Delta x} - e^{i\kappa (l-1) \Delta x}). \end{aligned} \tag{38}$$

Thus, the real wavenumber is given by  $\kappa = \frac{Z_1}{\Delta x}$  and the modified wavenumber is a result of the numerical approximation of  $Z_1$ , i.e.,  $\kappa^* = \frac{Z_1^*}{\Delta x}$ . Fig. 1 shows the dispersion and the dissipation errors of the proposed method. The dispersion error is associated to the difference between the modified and the real wavenumber and the dissipation is due to the imaginary part. As depicted in Fig. 1, when the reconstruction order is increased, the range of resolved frequencies enlarges. Note that when the modified frequency does not match the real one, the scheme introduces numerical dissipation.

### 7.2. One-dimensional linear advection equation

The second validation numerical example is the linear convection of an entropy-wave that reads

$$\frac{\partial U}{\partial t} + a \frac{\partial U}{\partial x} = 0 \tag{39}$$

where  $a$  represents the convective velocity, which is constant and taken as  $a = 1$ . The computational domain is  $\Omega = [0, 4]$  and a set of structured meshes ranging from 16 to 512 control volumes is used to discretized it. In the boundaries, periodic conditions are applied. The variable  $U$  is initialized with the following expression

$$U_0 = 1 + 0.2 \sin(\pi x). \tag{40}$$

It must be emphasized that the accurate evaluation of the initial condition in the finite volume framework is a crucial point to reach a very high-order scheme. Using a point-wise value instead of a cell-averaged value introduces a second order error,  $\mathcal{O}(h^2)$  as previously explained.

This benchmark is widely used to analyze the accuracy, formal order of convergence and efficiency of new formulations [45] since it has a known analytic solution, that is

$$U = 1 + 0.2 \sin(\pi(x - ta)). \tag{41}$$

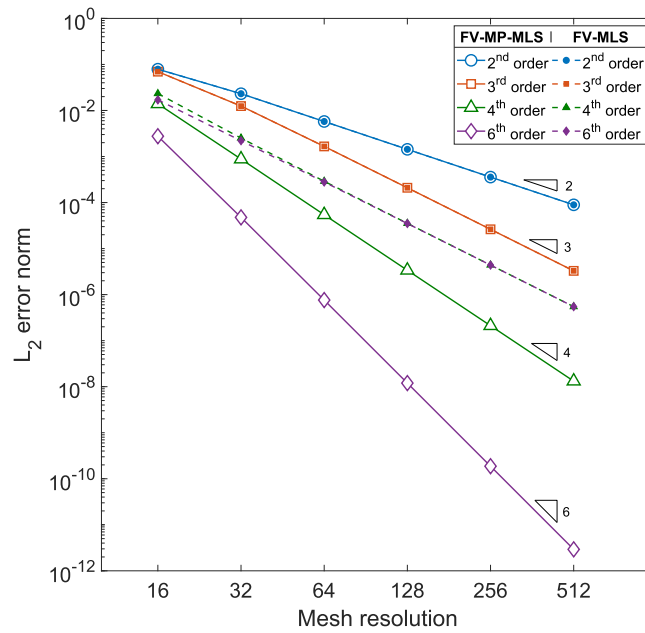


Fig. 2. 1D 1D linear advection equation: Comparison of the accuracy and formal order of FV-MLS (dashed lines) and the proposed FV-MP-MLS (solid lines).

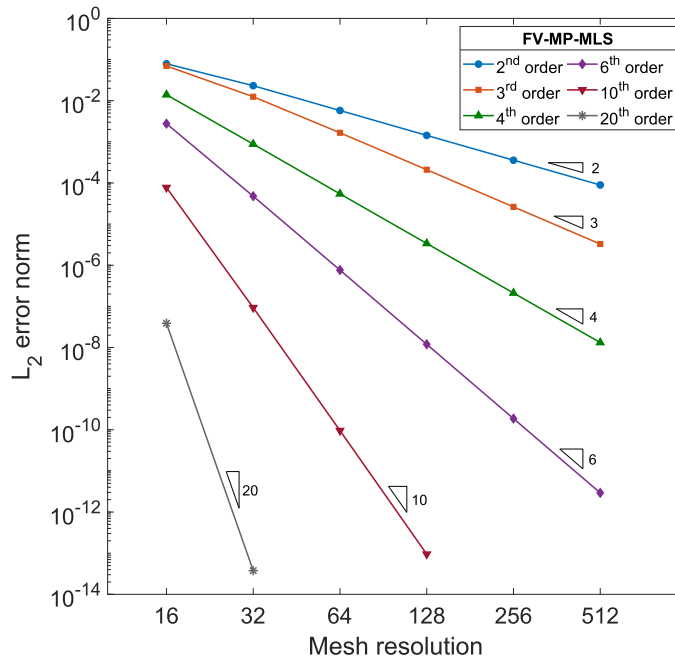


Fig. 3. 1D linear advection equation:  $L_2$  norm of the numerical error of the FV-MP-MLS for each mesh size and each order of approximation.

The simulation is run until  $t = 4$ . In order to study the effect of the new FV-MP-MLS compared with the traditional FV-MLS, the reconstructed values of  $U$  and the  $L_2$  norms are computed using both formulations (FV-MLS and FV-MP-MLS). In the former, from a third-order polynomial reconstruction the performance decreases drastically, not being able to surpass a third-order accuracy. In the latter, the expected formal order of accuracy is achieved (see Fig. 2).

In Fig. 3 the  $L_2$  norms are computed and plotted using the FV-MP-MLS with an order of reconstruction ranging from 2<sup>nd</sup> to 20<sup>th</sup>. As depicted, when the order is increased, the computational error is remarkably reduced. Hence, given a desired accuracy, the use of a very high-order scheme allows us to significantly reduce the number of control volumes that discretizes the domain. For example, in this problem, same accuracy can be obtained using a tenth-order reconstruction using a grid 16 times coarser than the mesh required for a second-order approximation.

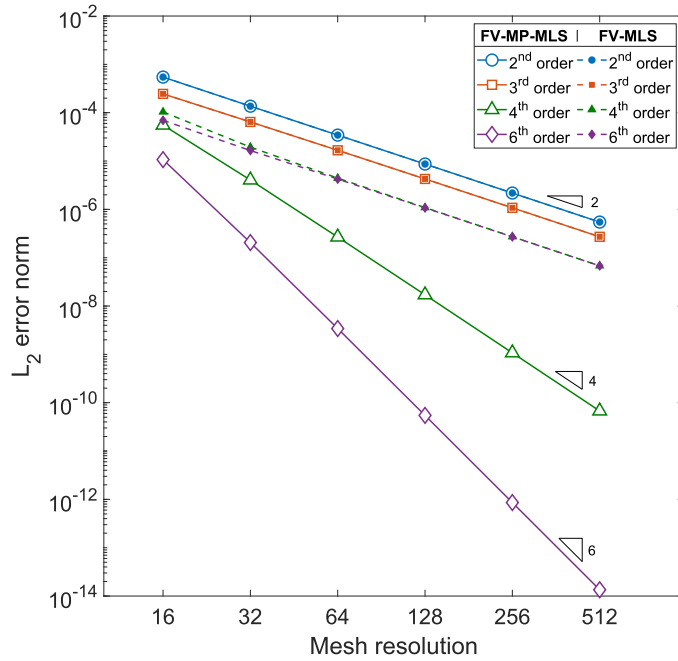


Fig. 4. 1D Convection-Diffusion equation: Comparison of the accuracy and convergence rate of FV-MLS (dashed lines) and the proposed FV-MP-MLS (solid lines).

**Table 1**  
1D Convection-Diffusion equation: FV-MLS error norms and convergence order results.

FV-MLS								
N	2 <sup>nd</sup> order		3 <sup>rd</sup> order		4 <sup>th</sup> order		6 <sup>th</sup> order	
	L <sub>2</sub>	O <sub>2</sub>						
16	5.46E-04	-	2.45E-04	-	1.04E-04	-	6.95E-05	-
32	1.36E-04	2.00	6.44E-05	1.93	1.94E-05	2.42	1.65E-05	2.07
64	3.44E-05	1.99	1.67E-05	1.65	4.43E-06	2.13	4.23E-06	1.96
128	8.67E-06	1.99	4.26E-06	1.95	1.09E-06	2.03	1.07E-06	1.98
256	2.18E-06	1.99	1.08E-06	1.98	2.71E-07	2.00	2.71E-07	1.99
512	5.46E-07	2.00	2.71E-07	1.99	6.80E-08	2.00	6.80E-08	2.00

### 7.3. One-dimensional Convection-Diffusion equation

This benchmark aims to validate the performance of the FV-MP-MLS to solve the convection-diffusion equation, which reads

$$\frac{\partial U}{\partial t} + a \frac{\partial U}{\partial x} - b \frac{\partial^2 U}{\partial x^2} = S \tag{42}$$

where  $a$  represents the constant free-stream velocity,  $b$  is the diffusivity and  $S$  denotes the source term. In this test case, we set  $a = 1$  and  $b = 1$ .

We manufacture the analytic solution for this equation on the computational domain  $\Omega = [0, 4]$  as

$$U = e^{-t} (1 + 0.2 \sin(\pi x)). \tag{43}$$

Introducing (43) in (42), we obtain the source term  $S$  that makes (43) the manufactured solution. Periodic boundary conditions are prescribed and the final time of the simulation is  $t = 4$ .

Again, the accurate evaluation of the source term and the initial condition is an important aspect in obtaining the desired accuracy and convergence rate. The finite volume discretization (equation 9) requires the integral value of the source term.

As depicted in Fig. 4 the expected convergence rate is only achieved for the FV-MP-MLS method. However, when the FV-MLS method is applied, the convergence rate remains second order, as expected. The  $L_2$  norms of error and the convergence orders  $O_2$  for the variable  $U$  are reported in Tables 1 and 2.

**Table 2**  
1D Convection-Diffusion equation: FV-MP-MLS error norms and convergence order results.

FV-MP-MLS									
N	2 <sup>nd</sup> order		3 <sup>rd</sup> order		4 <sup>th</sup> order		6 <sup>th</sup> order		
	L <sub>2</sub>	O <sub>2</sub>							
16	5.46E-04	-	2.45E-04	-	5.54E-05	-	1.07E-05	-	
32	1.36E-04	2.00	6.44E-05	1.93	4.05E-06	3.77	2.06E-07	5.70	
64	3.44E-05	1.99	1.67E-05	1.95	2.68E-07	3.92	3.42E-09	5.91	
128	8.67E-06	1.99	4.26E-06	1.97	1.71E-08	3.97	5.46E-11	5.97	
256	2.18E-06	1.99	1.08E-06	1.98	1.08E-09	3.99	8.60E-13	5.99	
512	5.46E-07	2.00	2.71E-07	1.99	6.74E-11	3.99	1.35E-14	6.00	

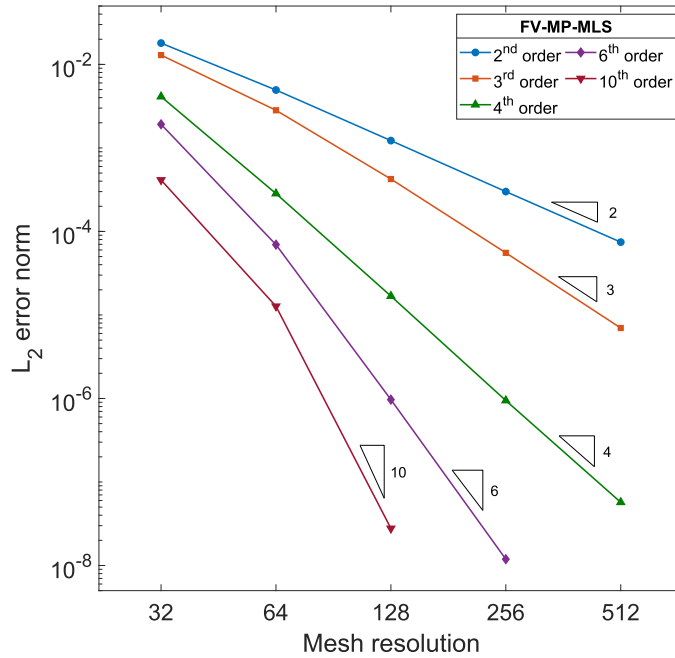


**Fig. 5.** 2D Euler equations. Isentropic Vortex Convection. L<sub>2</sub> norm of the numerical error in the pressure of the FV-MP-MLS for each mesh size and each order of approximation.

7.4. Two-dimensional Euler equations: Isentropic Vortex Convection

In this numerical example, the Euler equations are analyzed in two dimensions. To validate the proposed formulation we solve the Isentropic Vortex Convection test case, that is extensively used in the literature to analyze the accuracy order of numerical methods [35,46–48]. The initial condition and the analytical solution of this problem can be found in [35,48]. To evaluate the formal order of accuracy we adopt the following parameters:  $\alpha = 1$ ,  $(u_\infty, v_\infty) = (2, 0)$ ,  $\rho_\infty = 1$ ,  $p_\infty = 1$ ,  $(x_0, y_0) = (5, 5)$  and  $K = 5$ .

The domain is a square of size 10 and the vortex is located initially in the center of the domain. The periodic boundary conditions are set. In this test case, different mesh resolutions and reconstructions are tested, ranging from  $32^2$  to  $512^2$  finite volumes and from second to tenth order.

The simulation is run until the vortex reaches the initial position after a complete loop through the computational domain, that is  $t = 5$ .

The results of L<sub>2</sub> norm of the pressure error for different mesh resolutions and reconstruction orders and their corresponding rates of convergence are found in Fig. 5, where we remark that the formal order of accuracy is recovered for all the reconstructions. The obtained values are reported in Table 3.

7.5. Three-dimensional Euler equations: Inviscid Taylor Green Vortex

In this numerical example we solve the 3-D Euler equations. The numerical benchmark used to check the ability of the proposed method to deal with turbulent flow is the Taylor-Green vortex (TGV) test case. In this first 3D benchmark, we start with the inviscid one, which has a Reynolds number  $Re = \infty$ . This numerical example allows us to analyze the

**Table 3**  
2D Euler equations. Isentropic Vortex Convection: FV-MP-MLS error norms and convergence order results.

FV-MP-MLS						
N	2 <sup>nd</sup> order		3 <sup>rd</sup> order		4 <sup>th</sup> order	
	L <sub>2</sub>	O <sub>2</sub>	L <sub>2</sub>	O <sub>2</sub>	L <sub>2</sub>	O <sub>2</sub>
32 <sup>2</sup>	1.80E-02	-	1.30E-02	-	4.11E-03	-
64 <sup>2</sup>	4.94E-03	1.87	2.82E-03	2.20	2.84E-04	3.86
128 <sup>2</sup>	1.22E-03	2.01	4.24E-04	2.74	1.68E-05	4.08
256 <sup>2</sup>	3.00E-04	2.03	5.54E-05	2.94	9.44E-07	4.16
512 <sup>2</sup>	7.45E-05	2.01	6.98E-06	2.99	5.71E-08	4.05

FV-MP-MLS				
N	6 <sup>th</sup> order		10 <sup>th</sup> order	
	O <sub>2</sub>	L <sub>2</sub>	O <sub>2</sub>	L <sub>2</sub>
32 <sup>2</sup>	1.92E-03	-	4.13E-04	-
64 <sup>2</sup>	6.94E-05	4.79	1.27E-05	5.02
128 <sup>2</sup>	9.68E-07	6.16	2.78E-08	8.84
256 <sup>2</sup>	1.19E-08	6.35	-	-

nonlinear transfer of the kinetic energy in the scales of the flow. With this configuration, we can test the behavior of the numerical scheme performing LES in under-resolved flow simulations.

To simulate this case, we solve the three-dimensional compressible Euler equations in a periodic cube domain of  $[0, 2\pi]^3$ . The initial condition is given by

$$\begin{aligned}
 \rho_0 &= 1 \\
 u_0 &= \sin(x) \cos(y) \cos(z) \\
 v_0 &= -\cos(x) \sin(y) \cos(z) \\
 w_0 &= 0 \\
 p_0 &= 100 + \frac{[(\cos(2x) + \cos(2y))(2 + \cos(2z)) - 2]}{16}.
 \end{aligned} \tag{44}$$

We test the performance of the 6<sup>th</sup> order FV-MP-MLS with several grid discretizations: 32<sup>3</sup>, 64<sup>3</sup>, 128<sup>3</sup> and 256<sup>3</sup> cells. The simulation is run until  $t = 10$ . In this case the Roe's flux is used and the ratio of specific heat is  $\gamma = 1.4$ .

In Fig. 6 we show the temporal evolution of the normalized total kinetic energy for the previously mentioned discretizations. The theoretical kinetic energy is not decreasing due to the inviscid character of the test case. However, as the scales of the flow become smaller the numerical dissipation starts to act. In that moment, the problem becomes an isotropic decay of turbulent flow, where it is expected to follow Kolmogorov's law.

In this example, following [10] no turbulence model has been used for the computations. Here, the numerical dissipation acts as a subgrid scale model, following an implicit LES approach. Notice that, when very low dissipation schemes are used in under-resolved configurations, it could be possible that the amount of dissipation introduced would not be enough to mimic the physical process of decayment. In that case, additional dissipation should be added using explicit turbulence models or other numerical approach [12,26].

As expected, as the grid is refined, the solution keeps the energy constant for longer times. The discretization of 32<sup>3</sup> seems to be too coarse, since it starts the decay very soon, which is an indication of the existence of under-resolved scales on the solution.

This is confirmed analyzing the kinetic energy-spectrum. In Fig. 7 the energy spectrum is represented for the different mesh discretizations at  $t = 10$ . Within the inertial subrange, around  $t \approx 9$  [49], it is known that isotropic turbulence develops following the  $-5/3$  decay Kolmogorov's law of the kinetic-energy spectra for large Reynolds numbers. All the discretizations, except the coarser one are able to reproduce the inertial subrange. We remark that there is no pile-up in the kinetic energy. As the grid is refined, the inertial range also increases. As expected, all of them introduce dissipation in the highest wavenumbers, but this is the expected behavior in a candidate method for implicit LES.

Next, the enstrophy is analyzed. The local computation is performed as the square of the vorticity  $\omega = \nabla \times \mathbf{u}$  [54]. The temporal evolution of the integrated enstrophy on the domain  $\Omega$  reads as

$$\mathcal{E} = \frac{1}{2\rho_0\Omega} \int_{\Omega} \rho \omega_i \omega_i d\Omega. \tag{45}$$

In Fig. 8 we represent the obtained values of the enstrophy. We compare our results with those presented in [50], which are obtained using a semi-analytical method. It is noticeable the effect of increasing grid resolution. As it increases, the enstrophy largely increases.

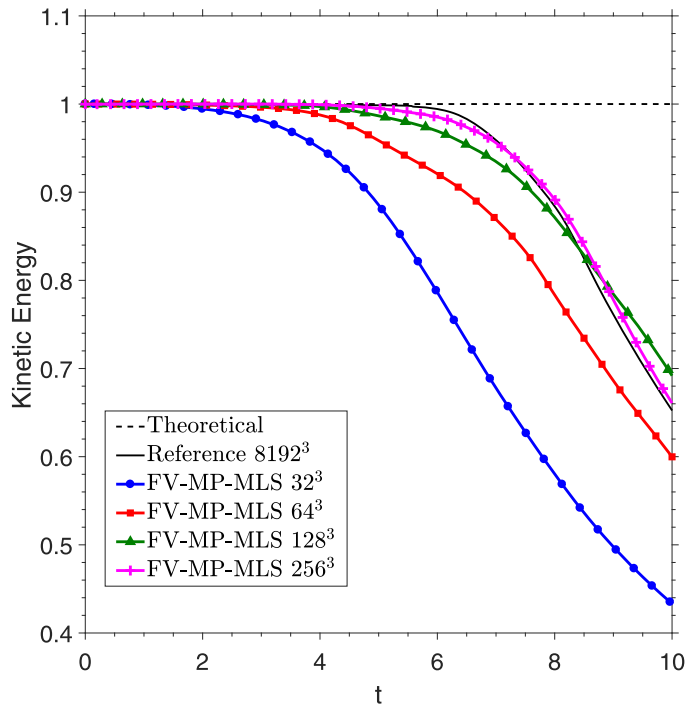


Fig. 6. 3D Euler equations. Inviscid TGV: Kinetic energy decay for different mesh resolutions for the 6<sup>th</sup> order FV-MP-MLS method.

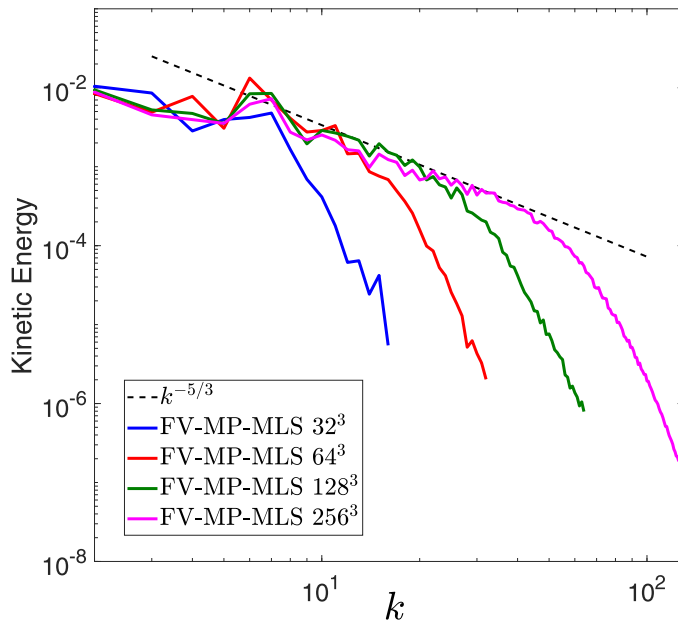


Fig. 7. 3D Euler equations. Inviscid TGV: Energy spectrum at  $t = 10$ . The solution is computed using a 6<sup>th</sup> order FV-MP-MLS with different mesh resolutions.

7.6. Three-dimensional Navier-Stokes equations: Taylor Green Vortex with  $Re = 1600$

In this last numerical example, the 3D Taylor-Green Vortex with  $Re = 1600$ , is analyzed. This benchmark is widely used to analyze the accuracy and performance of numerical methods for LES and Direct Numerical Simulation (DNS) of a 3D periodic and transitional flow [51,52].

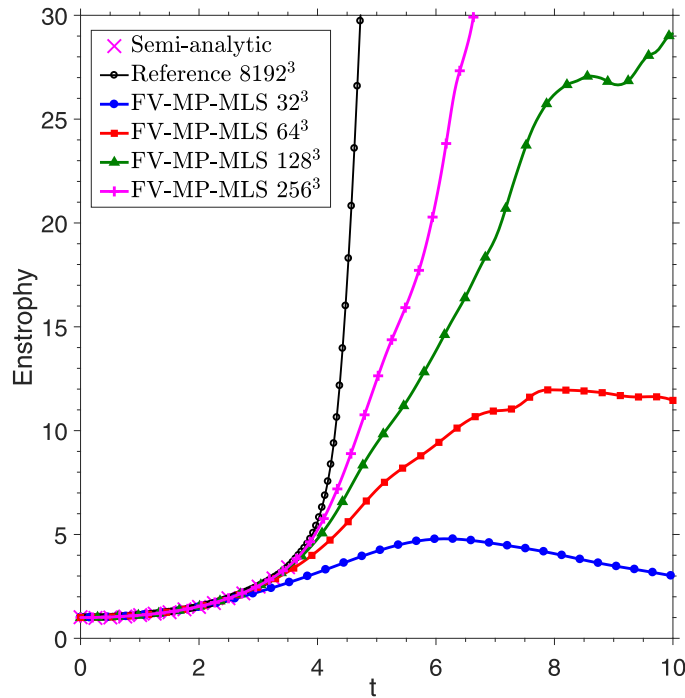


Fig. 8. 3D Euler equations. Inviscid TGV: Enstrophy time evolution for different mesh resolutions for the 6<sup>th</sup> order FV-MP-MLS method.

The compressible Navier-Stokes equations are solved. The problem’s domain is the same as in the inviscid case. The initial condition is defined as

$$\begin{aligned}
 \rho_0 &= \gamma M_0^2 p_0 \\
 u_0 &= \sin(x) \cos(y) \cos(z) \\
 v_0 &= -\cos(x) \sin(y) \cos(z) \\
 w_0 &= 0 \\
 p_0 &= \frac{1}{\gamma M_0^2} + \frac{[(\cos(2x) + \cos(2y))(2 + \cos(2z)) - 2]}{16}.
 \end{aligned}
 \tag{46}$$

As suggested in [52], since this case is designed to be computed with incompressible solvers, a reference Mach number of  $M_0 = 0.1$  is used to minimize the compressibility effects in the solution. In this test case,  $\gamma = 1.4$  and the Prandtl number is set to  $Pr = 0.71$

The temporal evolution of the kinetic energy is compared in Fig. 9 for the 6<sup>th</sup> order FV-MP-MLS method with different mesh resolutions, ranging from  $32^3$  to  $256^3$  until a final time of  $t = 10$ .

The results are compared with the WENO5 and WENO5 ADA schemes on a Finite Difference framework [26] with  $\gamma = 5/3$ , and also with a reference solution computed with  $512^3$  degrees of freedom using a pseudo-spectral incompressible flow solver [52,53]. WENO-ADA scheme is a WENO scheme with adaptive dissipation, specially designed to mimic Kolgomorov’s law in turbulence decay problems. As the mesh resolution is increased the obtained numerical solution converges to that reference solution. Furthermore, the proposed method achieves a more accurate solution than the WENO5 and the WENO5 ADA. Except for the two coarser grids, the decay rate is well captured by the simulations. This is more clearly shown in Fig. 10, where the dissipation rate, defined as  $\epsilon = -\frac{d E_k}{dt}$  is plotted. It is observed that the  $256^3$  grid obtains results that match very closely the reference solution.

The temporal evolution of the enstrophy defined in (45) is plotted in Fig. 11. As expected, it is seen that increasing the spatial resolution leads to higher peak of enstrophy, due to decreasing dissipation. Moreover, the scheme obtains a higher enstrophy than the WENO5 scheme for all the considered meshes. However, a significant improvement can be observed when the ADA method is used, particularly in the  $128^3$  mesh. It is worth pointing out that a similar approach could be applied to the FV-MP-MLS scheme, to adapt the intrinsic dissipation of the method to the characteristics of the flow. This will be addressed in forthcoming works.

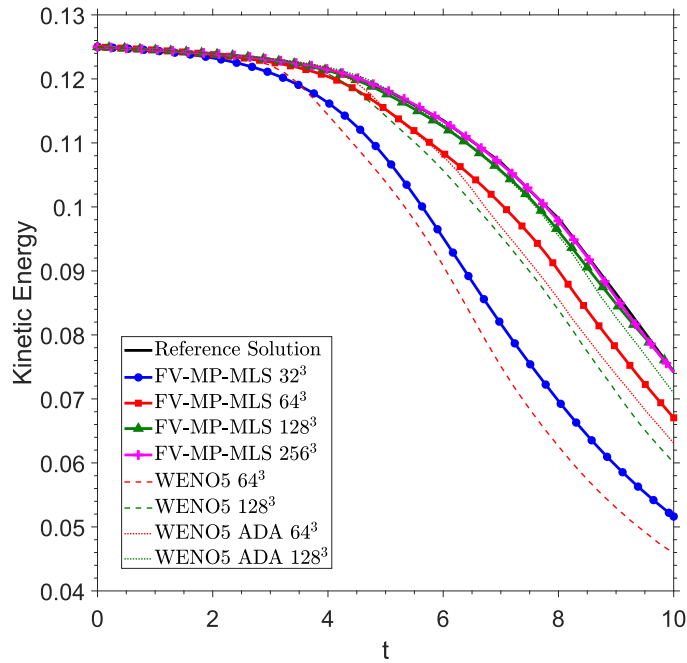


**Fig. 9.** 3D Navier-Stokes equations. TGV  $Re = 1600$ : Kinetic energy temporal evolution. The solutions are computed using a 6<sup>th</sup> order FV-MP-MLS method with mesh resolutions of  $32^3$ ,  $64^3$ ,  $128^3$ ,  $256^3$ . The reference solution is obtained from [52]. The WENO5 and WENO5 ADA results are taken from [26].

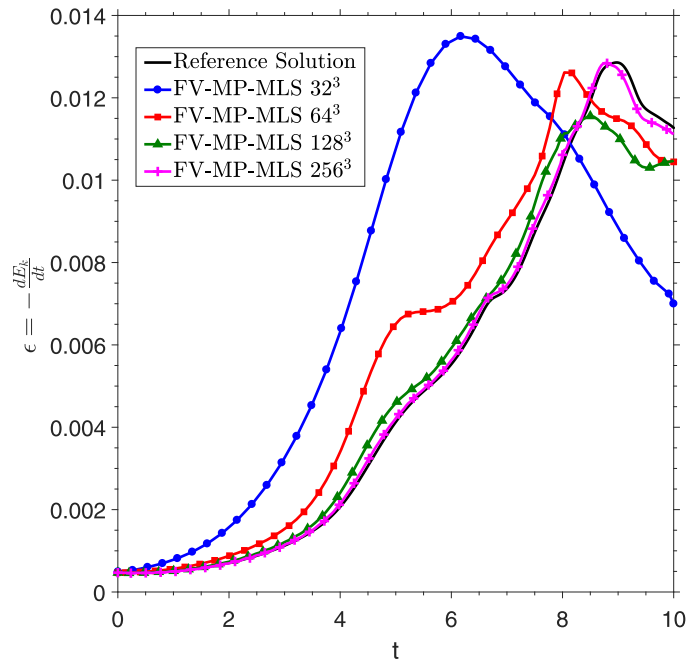


**Fig. 10.** 3D Navier-Stokes equations. TGV  $Re = 1600$ : Time evolution of the dissipation rate of the kinetic energy for the 6<sup>th</sup> order FV-MP-MLS method with mesh resolutions of  $32^3$ ,  $64^3$ ,  $128^3$ ,  $256^3$ . The reference solution is obtained from [52].

In Fig. 12, the instantaneous energy spectrum is shown for the dimensionless time  $t = 8$  for the different mesh resolutions. As the mesh resolution is increased the obtained energy spectrum converges to the reference solution. Except the coarser grid, the rest of discretizations are able to capture an inertial subrange. As in the inviscid case, it is also noticed an excessive dissipation in the highest wavenumbers for all the discretizations, and no pile-up is detected for any grid.

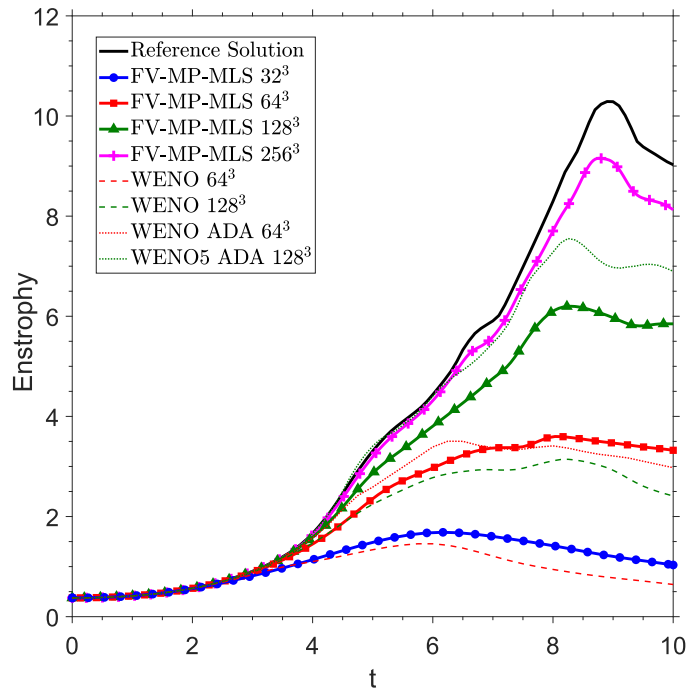


Fig. 11. 3D Navier-Stokes equations. TGV  $Re = 1600$ : Time evolution of the enstrophy for the 6<sup>th</sup> order FV-MP-MLS method with mesh resolutions of  $32^3$ ,  $64^3$ ,  $128^3$ ,  $256^3$ . The reference solution is obtained from [52]. The WENO5 and WENO5 ADA results are taken from [26].

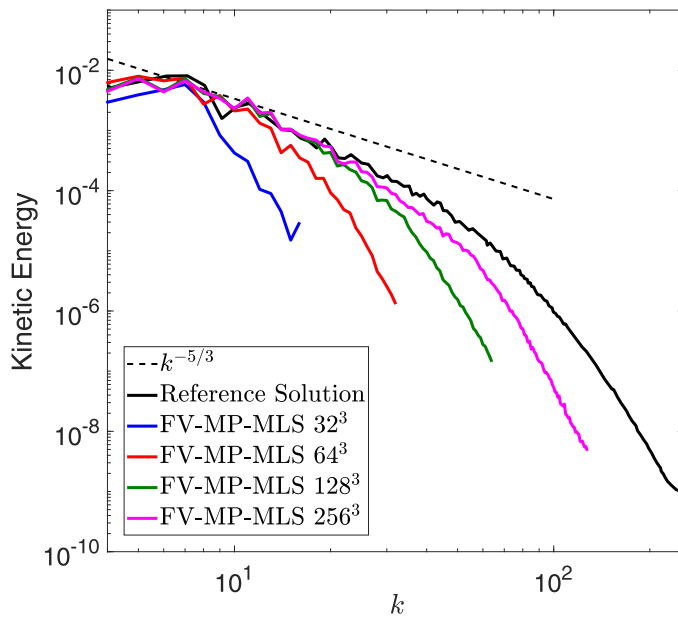
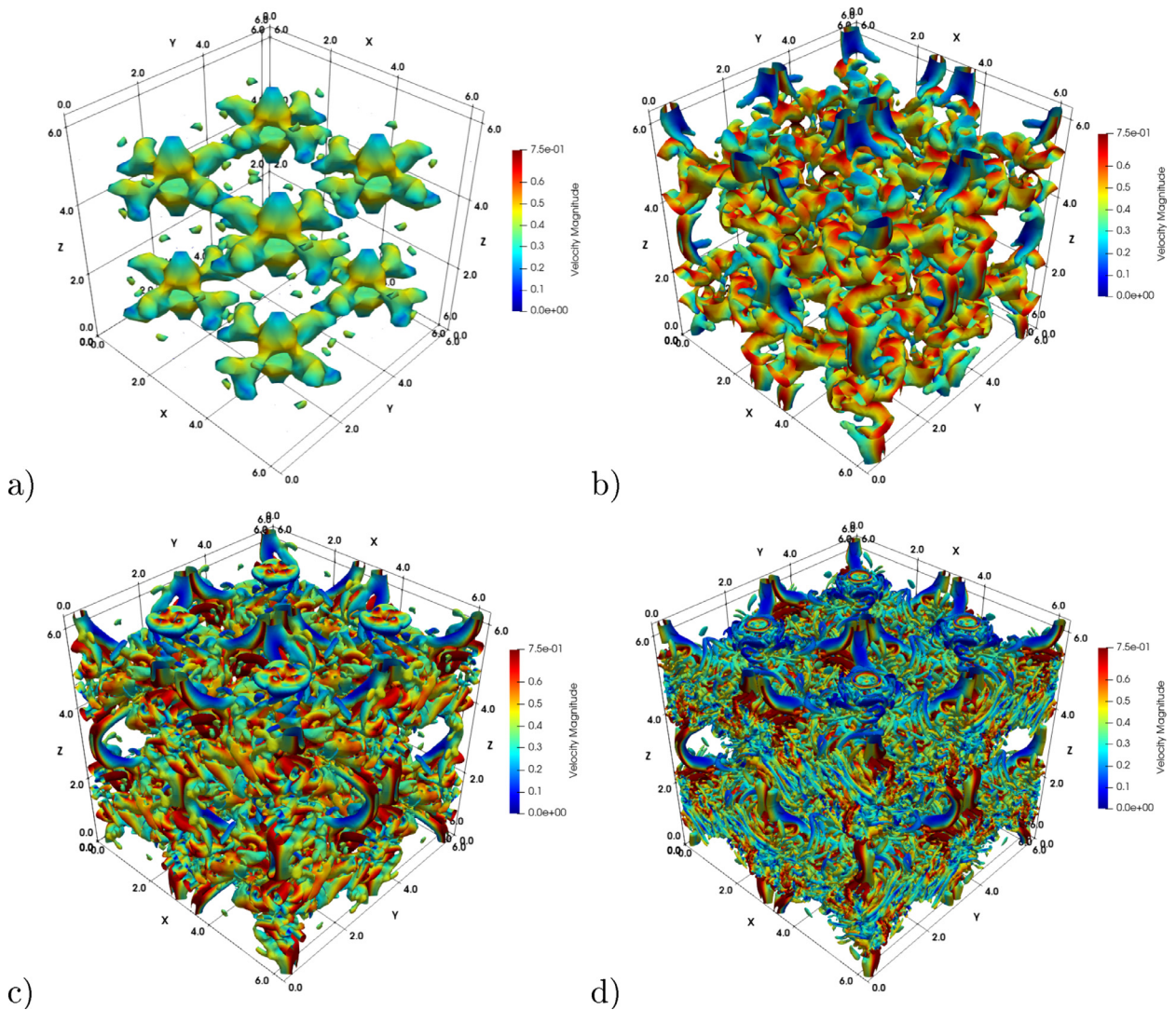


Fig. 12. 3D Navier-Stokes equations. TGV with  $Re = 1600$ : Instantaneous three-dimensional spectrum of the kinetic energy at  $t = 8$  for the 6<sup>th</sup> order FV-MP-MLS method with mesh resolutions of  $32^3$ ,  $64^3$ ,  $128^3$ ,  $256^3$ . The reference solution is obtained from [52].

The iso-surfaces of Q-Criterion with a value of 0.5 at  $t = 10$  are shown in Fig. 13 for the discretizations considered before. The color map indicates the magnitude of the velocity. The mesh resolution has a noticeable effect in the flowfield at the final time. The finer the mesh employed, the smaller the flow structures become. In particular, the coarser mesh ( $32^3$ ) exhibits large-scale flow patterns, while in the other grids the vortices have already broken down and the turbulence is developing.



**Fig. 13.** 3D Navier-Stokes equations. TGV  $Re = 1600$ : Iso-surfaces of  $Q$ -Criterion=0.5 at  $t = 10$  for the 6<sup>th</sup> order FV-MP-MLS method with mesh resolution of: a)  $32^3$ , b)  $64^3$ , c)  $128^3$  and d)  $256^3$ .

## 8. Conclusions

This paper proposes a modification to the error functional of Moving Least Squares approximations that allow us to obtain a new Finite Volume method (FV-MP-MLS) that is able to reach arbitrary order of accuracy on unsteady problems. The presented MP-MLS polynomial reconstruction is focused on the cell-averaged framework, as opposed to the point-wise approach of the traditional MLS method. As a result, the FV-MP-MLS method can be implemented straightforwardly in an existing FV-MLS code and its well-suited for application in unstructured grids. Furthermore, the numerical examples have shown that the new reconstruction method can obtain very high-orders of accuracy. Thus, the FV-MP-MLS seems suitable for its application to turbulent flow problems and other challenging and demanding cases, where high-order methods are indispensable to adequately resolve complex flow structures and the finer features of the flow.

## Data availability

Data will be made available on request.

## Acknowledgments

The authors gratefully acknowledge the funding provided by the *Ministerio de Ciencia e Innovación* of the Spanish Government (Grants# PID2021-125447OB-I00 and TED2021-129805B-I00) and by the *Xunta de Galicia* (grants# ED431C 2018/41, # ED431E 2018/11 and ED431C 2022/06). Funding for open access charge: Universidade da Coruña/CISUG.

## References

- [1] T. Schwartzkopff, C.D. Munz, E.F. Toro, ADER: High-order approach for linear hyperbolic systems in 2d, *Journal of Scientific Computing* 17 (2002) 231–240.
- [2] T. Schwartzkopff, M. Dumbser, C.D. Munz, Fast high order ADER schemes for linear hyperbolic equations, *Journal of Computational Physics* 197 (2004) 532–539.
- [3] S.J. Sherwin, J. Peiró, Mesh generation in curvilinear domains using high-order elements, *International Journal for Numerical Methods in Engineering* 53 (2002) 207–223.
- [4] Z.J. Wang, K. Fidkowski, R. Abgrall, F. Bassi, D. Caraeni, A. Cary, H. Deconinck, R. Hartmann, K. Hillewaert, H.T. Huynh, N. Kroll, G. May, P.O. Persson, B. van Leer, M. Visbal, High-order CFD methods: current status and perspective, *International Journal for Numerical Methods in Fluids* 72 (08) (2013) 811–845.
- [5] T.J. Barth, P.O. Frederickson, Higher order solution of the euler equations on unstructured grids using quadratic reconstruction, *AIAA Paper* 90 (1990) 0013.
- [6] H. Nishikawa, The QUICK scheme is a third-order finite-volume scheme with point-valued numerical solutions, *International Journal for Numerical Methods in Fluids* 93 (2021) 2311–2338.
- [7] L. Cueto-Felgueroso, I. Colominas, X. Nogueira, F. Navarrina, M. Casteleiro, Finite volume solvers and moving least-squares approximations for the compressible navier-stokes equations on unstructured grids, *Computer Methods in Applied Mechanics and Engineering* 196 (2007) 4712–4736.
- [8] P. Lancaster, K. Salkauskas, Surfaces generated by moving least squares methods, *Mathematics of Computation* 37 (155) (1981) 141–158.
- [9] L. Ramírez, X. Nogueira, J.C. Chassaing, S. Khelladi, I. Colominas, A new higher-order finite volume method based on moving least squares for the resolution of the incompressible navier-stokes equations on unstructured grids, *Computer Methods in Applied Mechanics and Engineering* 278 (2014) 883–901.
- [10] X. Nogueira, S. Khelladi, I. Colominas, L. Cueto-Felgueroso, J. París, H. Gómez, High-resolution finite volume methods on unstructured grids for turbulence and aeroacoustics, *Archives of Computational Methods in Engineering* 18 (2011) 315–340.
- [11] X. Nogueira, L. Cueto-Felgueroso, I. Colominas, S. Khelladi, On the simulation of wave propagation with a higher-order finite volume scheme based on reproducing kernel methods, *Computer Methods in Applied Mechanics and Engineering* 199 (23–24) (2010) 1471–1490.
- [12] X. Nogueira, L. Ramírez, J. Fernández-Fidalgo, M. Deligant, S. Khelladi, J.-C. Chassaing, F. Navarrina, An a posteriori-implicit turbulent model with automatic dissipation adjustment for large eddy simulation of compressible flows, *Computers & Fluids* 197 (2020) 104371.
- [13] S. Khelladi, X. Nogueira, F. Bakir, I. Colominas, Toward a higher-order unsteady finite volume solver based on reproducing kernel particle method, *Computer Methods in Applied Mechanics and Engineering* 200 (2011) 2348–2362.
- [14] P. Costa, D. Albuquerque, A novel approach for temporal simulations with very high-order finite volume schemes on polyhedral unstructured grids, *Journal of Computational Physics* 453 (2022) 110960.
- [15] C.F. Ollivier-Gooch, M.V. Alena, A high-order accurate unstructured mesh finite-volume scheme for the advection-diffusion equation, *Journal of Computational Physics* 181 (2) (2002) 729–752.
- [16] C.F. Ollivier-Gooch, A. Nejat, K. Michalak, On obtaining high-order finite-volume solutions to the euler equations on unstructured meshes, *AIAA 2007-4464*, 18th AIAA Computational Fluid Dynamics Conference (2007).
- [17] S. Clain, S. Diot, R. Loubère, A high-order finite volume method for systems of conservation laws-multi-dimensional optimal order detection (MOOD), *Journal of Computational Physics* 230 (2011) 4028–4050.
- [18] S. Clain, R. Loubère, S. Diot, The multidimensional optimal order detection method in the three-dimensional case: very high-order finite volume method for hyperbolic systems, *International Journal for Numerical Methods in Fluids* 73 (2013) 362–392.
- [19] E. Toro, A. Hidalgo, ADER finite volume schemes for nonlinear reaction-diffusion equations, *Applied Numerical Mathematics* 59 (1) (2009) 73–100.
- [20] V.A. Titarev, E.F. Toro, ADER schemes for three-dimensional non-linear hyperbolic systems, *Journal of Computational Physics* 204 (2005) 715–736.
- [21] C.Q. Hu, C.W. C. W. Shu, Weighted essentially non-oscillatory schemes on triangular meshes, *Journal of Computational Physics* 150 (1) (1999) 97–127.
- [22] O. Friedrich, Weighted essentially non-oscillatory schemes for the interpolation of mean values on unstructured grids, *Journal of Computational Physics* 144 (1) (1998) 194–212.
- [23] M. Dumbser, M. Köser, Arbitrary high order non-oscillatory finite volume schemes on unstructured meshes for linear hyperbolic systems, *Journal of Computational Physics* 221 (2) (2007) 693–723.
- [24] P. Tsoutsanis, A. Antoniadis, D. Drikakis, WENO schemes on arbitrary unstructured meshes for laminar, transitional and turbulent flows, *Journal of Computational Physics* 256 (2014) 254–276.
- [25] P. Tsoutsanis, M. Dumbser, Arbitrary high order central non-oscillatory schemes on mixed-element unstructured meshes, *Computers & Fluids* 225 (2021) 104961.
- [26] J. Fernández-Fidalgo, L. Ramírez, P. Tsoutsanis, I. Colominas, X. Nogueira, A reduced-dissipation WENO scheme with automatic dissipation adjustment, *Journal of Computational Physics* 425 (2021) 109749.
- [27] A. Gossler, Moving least-squares: a numerical differentiation method for irregularly spaced calculation points, *SANDIA Report, SAND2001* (2001) 1669.
- [28] D. Avesani, M. Dumbser, A. Bellin, A new class of moving-least-squares WENO-SPH schemes, *Journal of Computational Physics* 270 (2014) 278–299.
- [29] L. Ramírez, X. Nogueira, S. Khelladi, A. Krimi, I. Colominas, A very accurate arbitrary lagrangian-eulerian meshless method for computational aeroacoustics, *Computer Methods in Applied Mechanics and Engineering* 342 (2018) 116–141.
- [30] D. Avesani, M. Dumbser, R. Vacondio, M. Righetti, An alternative SPH formulation: ADER-WENO-SPH, *Computer Methods in Applied Mechanics and Engineering* 382 (2021) 113871.
- [31] R. Antona, R. Vacondio, D. Avesani, M. Righetti, M. Renzi, Towards a high order convergent ALE-SPH scheme with efficient WENO spatial reconstruction, *Water*, 13, 2432, 2021.
- [32] B. Nayroles, G. Touzot, P. Villon, Generalizing the finite element method: Diffuse approximation and diffuse elements, *Computational Mechanics* 10 (5) (1992) 307–318.
- [33] T. Belytschko, Y. Krongauz, D. Organ, M. Fleming, P. Krysl, Meshless methods: An overview and recent developments, *Computer Methods in Applied Mechanics and Engineering* 139 (1996) 3–47.
- [34] L. Cueto-Felgueroso, I. Colominas, High-order finite volume methods and multiresolution reproducing kernels, *Archives of Computational Methods in Engineering* 15 (2) (2008) 185–228.
- [35] L. Ramírez, X. Nogueira, P. Ouro, F. Navarrina, S. Khelladi, I. Colominas, A higher-order chimera method for finite volume schemes, *Archives of Computational Methods in Engineering* 25 (3) (2018) 691–706.
- [36] G.R. Liu, M.B. Liu, *Smoothed Particle Hydrodynamics*. A meshfree particle method, World Scientific Publishing, Singapore, 2003.
- [37] Y. Liu, M. Vinokur, Z.J. Wang, Spectral (finite) volume method for conservation laws on unstructured grids v: Extension to three-dimensional systems, *Journal of Computational Physics* 212 (2006) 454–472.

- [38] T. Most, C. Bucher, New concepts for moving least squares: An interpolation non-singular weighting function and weighted nodal least square, *Engineering Analysis with Boundary Elements* 32 (2008) 461–470.
- [39] X. Nogueira, L. Ramirez, S. Khelladi, J.C. Chassaing, I. Colominas, A high-order density-based finite volume method for the computation of all-speed flows, *Computer Methods in Applied Mechanics and Engineering* 298 (2016) 229–251.
- [40] J.C. Chassaing, S. Khelladi, X. Nogueira, Accuracy assessment of a high-order moving least squares finite volume method for compressible flows, *Computers & Fluids* 71 (2013) 41–53.
- [41] V.V. Rusanov, The calculation of the interaction of non-stationary shock waves and obstacles, *USSR Computational Mathematics and Mathematical Physics* 1 (2) (1962) 304–320.
- [42] P.L. Roe, Approximate riemann solvers, parameter vectors and difference schemes, *Journal of Computational Physics* 43 (1981) 357–372.
- [43] C.W. Shu, S. Osher, Efficient implementation of essentially nonoscillatory shock-capturing schemes, *Journal of Computational Physics* 77 (1998) 439–471.
- [44] D. Ghosh, J.D. Baeder, Compact reconstruction schemes with weighted ENO limiting for hyperbolic conservation laws, *SIAM Journal on Scientific Computing* 34 (3) (2012) A1678–A1706.
- [45] J.C. Hardin, J.R. Ristorcelli, C.K.W. Tam, ICASE/LaRC workshop on benchmark in computational aeroacoustic, 3300, NASA Conference Publication, 1995.
- [46] G. Wang, F. Duchaine, D. Papadogiannis, I. Duran, S. Moreau, L.Y.M. Gicquel, An overset grid method for large eddy simulation of turbomachinery stages, *Journal of Computational Physics* 274 (2014) 333–355.
- [47] K.R. Lee, J.H. Park, K.H. Kim, High-order interpolation method for overset grid based on finite volume method, *AIAA Journal* 49 (2011) 1387–1398.
- [48] L. Ramírez, C. Foulquié, X. Nogueira, S. Khelladi, J.C. Chassaing, I. Colominas, New high-resolution-preserving sliding mesh techniques for higher-order finite volume schemes, *Computers & Fluids* 118 (2015) 114–130.
- [49] D. Fauconnier, C. De Langhe, E. Dick, Construction of explicit and implicit dynamic finite difference schemes and application to the large-eddy simulation of the taylor-green vortex, *Journal of Computational Physics* 228 (21) (2009) 8053–8084.
- [50] M.E. Brachet, D.I. Meiron, S.A. Orszag, B.G. Nickel, R.H. Morf, U. Frisch, Small-scale structure of the taylor-green vortex, *Journal of Fluid Mechanics* 130 (1983) 411–452.
- [51] D.J. Lusher, N.D. Sandham, Assessment of low-dissipative shock-capturing schemes for the compressible taylor-green vortex, *AIAA Journal* 59 (2) (2021) 533–545.
- [52] HiOCFD5, 5th International Workshop on High-Order CFD Methods, (14<sup>th</sup>, June, 2022), WS1 DNS of the Taylor-Green vortex at  $Re = 1600$ , <https://www.how5.cenaero.be/content/ws1-dns-taylor-green-vortex-re1600>.
- [53] D.J. Garmann, M.R. Visbal, AFRL contributions to the third international workshop on high-order CFD methods, Third International Workshop on High-Order CFD Methods (2015).
- [54] Z.J. Wang, K. Fidkowski, R. Abgrall, F. Bassi, D. Caraeni, A. Cary, H. Deconinck, R. Hartmann, K. Hillewaert, H.T. Huynh, N. Kroll, G. May, P. Persson, M. Visbal, B. van Leer, High-order CFD methods: current status and perspective, *Numerical Methods in Fluids* 72 (2013) 811–845.